Desalination 586 (2024) 117859

Contents lists available at ScienceDirect

Desalination

journal homepage: www.elsevier.com/locate/desal

Reverse osmosis reject water management by immobilization into alkali-activated materials

Sima Kamali [a], Vitalii Ponomar [a], Giovanni Dal Poggetto [b], Cristina Leonelli [b], Katja Kilpimaa [a], Tero Luukkonen [a,c,*]

[a] University of Oulu, Fiber and Particle Engineering Research Unit, P.O. Box 8000, 90014, Finland
[b] Department of Engineering "Enzo Ferrari", University of Modena and Reggio Emilia, Via P. Vivarelli 10, 41125 Modena, Italy
[c] Department of Chemical Engineering Technology, University of Johannesburg, P.O. Box 17011, Doornfontein 2088, South Africa

HIGHLIGHTS

- Alkali-activated materials (AAMs) were prepared using high-salinity waters.
- AAMs prepared using blast furnace slag immobilized salts effectively.
- AAMs containing metakaolin had a higher level of salt leaching.
- Immobilization involved both chemical and physical mechanisms.
- High salt content enhanced the formation of high-strength material.

GRAPHICAL ABSTRACT

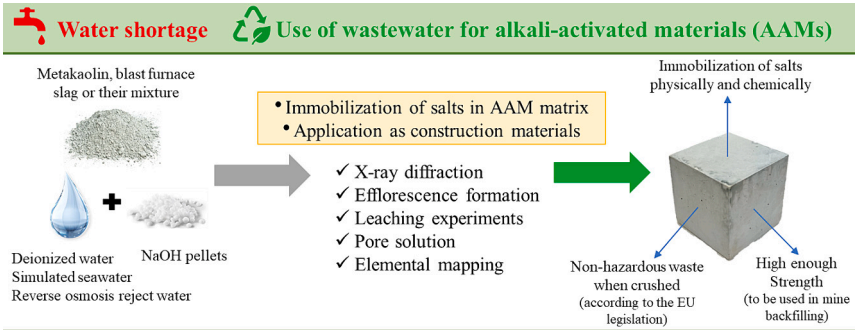

ARTICLE INFO

Keywords:
Alkali-activated materials
Geopolymer
Salinity
Solidification/stabilization
Wastewater

ABSTRACT

Water-intensive industries face challenges due to water scarcity and pollution. In the management of these challenges, membrane processes play an important role. However, they produce significant amounts of reject waters, in which the separated salts and pollutants are concentrated. This study aims to develop a novel management concept for reject waters using alkali activation to immobilize salts in a solid phase using metakaolin, blast furnace slag (BFS), or their mixture as precursors and to create alkali-activated materials with sufficient properties to be potentially used in construction applications. Seven different waters were used to prepare the NaOH-based alkali activator solution: deionized water, three simulated seawaters with increasing salinity, and three reverse osmosis (RO) reject waters from mining or pulp and paper industries. Overall, BFS-based samples had the highest immobilization efficiency, likely due to the formation of layered double hydroxide phases (hydrotalcite, with anion exchange capacity) and hydrocalumite (chloride-containing mineral). Moreover, high-salinity water enhanced the dissolution of precursors, prolonged the setting time, and increased the compressive strength compared with nonsaline water. Thus, the obtained materials could be used in construction applications, such as backfilling material at mines where RO concentrates are commonly produced.

* Corresponding author at: University of Oulu, Fiber and Particle Engineering Research Unit, P.O. Box 8000, 90014, Finland.
E-mail address: tero.luukkonen@oulu.fi (T. Luukkonen).

https://doi.org/10.1016/j.desal.2024.117859
Received 4 December 2023; Received in revised form 31 May 2024; Accepted 16 June 2024
Available online 26 June 2024

1. Introduction

Water scarcity is a significant problem in many areas globally. One important user of freshwater resources is the concrete production industry, which was estimated to consume 16.6 Gt of water in 2012 [1]. Thus, the use of seawater or different wastewaters as batching water in concrete products could help to reduce the freshwater consumption if corrosion-prone metal rebars are not used [2]. Additionally, the management of many industrial wastewaters is a major environmental issue, where membrane separation processes, such as reverse osmosis (RO), are widely used. However, membrane processes produce reject water (also known as the rejectate or brine) in which the separated salts and other impurities are concentrated. For a typical RO process, the amount of reject water can be up to 80 % depending on the influent salinity and applied pressure [3]. Currently, reject waters are further concentrated and discharged into seas, deep wells, evaporation ponds, or municipal sewers [4]. However, these methods are often not environmentally sustainable or practically and economically feasible, especially if the RO plant is located inland [5]. As an alternative approach, the immobilization of reject waters and other highly concentrated salt solutions into a solid matrix would decrease environmental contamination. One option for such a solid matrix could be alkali-activated materials (AAMs) [6,7].

AAMs are obtained through a reaction between aluminosilicate precursors (e.g., metakaolin [MK] or blast furnace slag [BFS]) and alkali activators (e.g., NaOH). They are separated into two classes depending on the products formed in the reaction: (1) those rich in calcium (i.e., CaO content <30 weight-%) and (2) those poor in calcium, which are referred to as geopolymers (i.e., CaO content <5 weight-%) [8]. The use of side stream materials for AAM production is not only affordable but also environmentally friendly. The mechanical properties and durability of AAMs produced using industrial side streams show that these materials have a high potential for application as construction materials [9,10].

AAMs are capable of binding solid wastes (frequently referred to as solidification/stabilization, S/S) in their structure via physical or chemical mechanisms to decrease the release of hazardous components (such as potentially toxic elements or ions) [11]. For instance, BFS-based AAMs have been used for the S/S and treatment of landfill leachate with immobilization rates of total organic carbon, chemical oxygen demand, NH_3–N, Cl^-, and SO_4^{2-} of 81 %, 89 %, 97 %, 97 %, and 78 %, respectively [12]. The addition of landfill leachate improved the alkali activation reaction [12]. Waste materials can have different functions in AAMs: those with soluble Al^{3+} or Si^{4+} can be used as precursors or those with the capability to increase pH can replace alkali activators [9,13,14]. Also, as mentioned earlier, the water used to prepare AAMs can be of waste origin or seawater to preserve freshwater resources. Some industrial wastewaters, such as those from copper mining or paper and pulp production, and seawater have been successfully used in AAMs [2,15,16]. The S/S of highly concentrated saline or other types of wastewater into a geopolymer matrix (sometimes referred to as inter-solidification) has been studied earlier up to the proof-of-concept level [17,18]. However, there are still significant knowledge gaps regarding the physicochemical mechanisms and practical applications of the S/S method [19]. Therefore, in this study, a novel concept of immobilizing highly concentrated saline wastewaters, such as RO reject waters, into AAMs is assessed. Furthermore, this study evaluates actual RO concentrate effluents in addition to simulated effluents to validate the method. The objectives of this study were to (1) compare MK, BFS, and their mixture (representing low, high, and medium-Ca systems, respectively) as precursors in high-salinity water-containing AAMs and (2) determine salt leaching and assess the fate of salts (i.e., the immobilization mechanism) in the AAMs. Three different binder systems were studied, and the optimal amount of alkali activator was screened. Then, six different high-salinity waters were used to replace deionized water. To identify the sinks of salts, X-ray diffraction (XRD) of the hardened pastes and efflorescence, leaching experiments, pore solution analysis, and elemental mapping were performed using an electron probe microanalyzer (EPMA). Suitability of prepared AAMs as a construction material was assessed in terms of compressive strength and setting time.

2. Materials and methods

2.1. Materials

Three types of precursors were used: MK (MetaMax, BASF, Germany), BFS (KJ400, Finnsementti, Finland), and a mixture of MK and BFS (1:2 as a weight ratio, respectively). The composition and XRD patterns of the precursors are shown in Table 1 and Fig. S1, respectively.

To prepare sodium hydroxide solutions, seven types of waters were used: (1) synthetic seawater prepared according to the standard ASTM D1141-98 [20], (2) synthetic seawater with a double concentration of salts, (3) synthetic seawater with a triple concentration of salts, (4) RO reject water from the mining industry, (5) and (6) two different RO reject waters from pulp and paper industries, and (7) deionized water (as a reference). The salts used to prepare the synthetic seawater were $MgCl_2{\cdot}6H_2O$ (VWR), $CaCl_2$ (anhydrous) (VWR), $SrCl_2{\cdot}6H_2O$ (VWR), KCl (Merck), $NaHCO_3$ (Merck), KBr (VWR), H_3BO_3 (Merck), NaF (VWR), NaCl (Sigma), and Na_2SO_4 (Sigma). The characteristics of the waters are shown in Table 2.

2.2. Preparation of the AAM samples

First, the sodium hydroxide tablets were mixed in different waters (Table 2) and cooled for 3 h. Then, the alkali activator was mixed with the precursors according to the ratios shown in Table 3. In addition, the NaOH content of the mix designs was optimized using deionized water (shown in Fig. S2). The mix designs containing MK, a mixture of MK and BFS, and BFS are referred to as low, medium, and high-Ca systems, respectively. After mixing, the fresh-state paste was cast into 20 × 20 × 20 mm^3 or 50 × 50 × 50 mm^3 cubic molds (depending on the intended analysis). The samples in the molds were covered with plastic bags for 24 h, then demolded, and kept in plastic bags until testing. Sample preparation and storage were conducted at room temperature (~22 °C).

2.3. Characterization of AAMs

2.3.1. Mechanical, microstructural and chemical characterization

Compressive strength was determined for 20 × 20 mm^2 area by using 1 mm/min loading rate and 5 N preload with a Zwick/Roell Z010 or Z100 universal testing machines. The compressive strength was calculated by dividing the force at break by the surface area.

Setting time was recorded by an automatic Vicat machine, model E044 N, by Matest.

A 4-kV wavelength-dispersive X-ray fluorescence spectrometer (PANalytical AxiosmAX) was used to determine the chemical composition of BFS and MK. The measurement was conducted on compacted powder. The loss on ignition of BFS and MK was determined by the mass decrease of a dried sample (at 105 °C for 24 h to reach constant weight) when heated to 950 °C.

XRD analysis was conducted with a Rigaku SmartLab diffractometer (9 kW Cu X-ray source) in the range of 5–120°2θ at a scan speed of 6°2θ/min to identify the crystalline phases from a 28-day-old sample. The hardened samples were milled before analysis.

Table 1
Oxide composition of the precursors.

Precursor	SiO_2 (wt%)	Al_2O_3 (wt%)	CaO (wt %)	SO_3 (wt %)	MgO (wt%)	Fe_2O_3 (wt%)	TiO_2 (wt%)
MK	49.8	42.0	0.0	0.0	–	0.4	1.7
BFS	29.1	11.5	32.4	3.5	11.1	0.4	2.0

An EPMA, Jeol JXA-8530F Plus with an energy-dispersive detector, was used for elemental mapping to qualitatively assess the composition of the formed gels and dissolution of the precursor particles. Crushed pieces of 28-day-old pastes were embedded in epoxy resin (EpoxiCure 2 Epoxy Resin and Epoxy Hardener, Buehler), polished with silicon carbide grinding papers (P240, P800, P1200, and 2000), and covered with carbon. The probe had a concentrated spot, 15 kV accelerating voltage, 20 nA current, 0.5 μm step size, and 500 ms dwell duration. Na^{+}, Ca^{2+}, S, and Cl were mapped.

2.3.2. Efflorescence and leaching of salts

Efflorescence formation was observed visually by placing a 50 × 50 × 50 mm^3 sample (cured for 28 days in plastic bags before the efflorescence test) into deionized water (half exposed in water and half in air) for 28 days. After exposure, the samples were photographed, and the formed efflorescence deposits were collected for XRD analysis.

To investigate the capacity of pastes to immobilize salts, two leaching experiments were conducted. The first method is based on a standard one-stage batch leaching test (SFS-EN 12457-2) and was used to measure leaching from crushed 28-day-old hardened samples (particle size <4 mm). The extraction was conducted with distilled water at a liquid/solid (L/S) mass ratio of 10 for 24 h. The weight of the crushed mortar was 87.5 g. Eluates were filtered with a 0.45 μm membrane filter, and the total concentrations of Na^{+}, Mg^{2+}, and Ca^{2+} (i.e., the main cations present in the studied waters) were measured with a Thermo Fisher Scientific iCAP 6500 Duo inductively coupled plasma optical emission spectrometer. Anions, SO_4^{2-} and Cl^{-}, were measured with an ion-chromatography system (ICS-2000, Dionex). Eq. (1) was used to calculate the leaching per dry mass (A_{10} = the release of a constituent at an L/S = 10 [mg/kg]; C_{10} = the concentration of a constituent in the eluate [mg/L]; L_{10} = the volume of the leachant [L]; MC = the moisture percentage of the dry mass).

$$A_{10} = C_{10}\left(\frac{L_{10}}{M_D} + \frac{MC}{100}\right) \quad (1)$$

The second leaching test was performed using a standard method for monolithic building materials (NEN 7343:1995). Cubic samples (50 × 50 × 50 mm^3) were exposed to 1 L of deionized water in closed containers at room temperature (+21 °C), and the water was replaced and sampled after 6 h, 24 h, 5 days, 16 days, 36 days, and 78 days. The leaching of a component per unit area (mg/m^2) was calculated according to Eq. (2), where c_i is the concentration of the component (mg/L), V is the volume of the eluate (L), and A is the surface area of the sample (m^2). Leaching was calculated as a cumulative value for up to 78 days.

$$E_i^{*} = \frac{C_i \times V}{A} \quad (2)$$

Table 3
Experimental mix designs for alkali-activated samples.

Sample ID	Water type	Mix design			
		MK [g]	BFS [g]	NaOH [g]	Water [g]
MK1	Deionized water	100	0	13.3	102
MK2	Deionized water	100	0	19.92	102
MK3	Deionized water	100	0	26.51	102
MK4	Deionized water	100	0	32.93	102
3M7B	Deionized water	33	67	13.56	59.3
BFS1	Deionized water	0	100	2.58	38
BFS2	Deionized water	0	100	3.87	38
BFS3	Deionized water	0	100	5.16	38
BFS4	Deionized water	0	100	6.45	38
MKS1	Seawater (1×)	100	0	32.93	102
MKS2	Seawater (2×)	100	0	32.93	102
MKS3	Seawater (3×)	100	0	32.93	102
MKRT	Mining industry RO reject	100	0	32.93	102
MKR1	Pulp and paper industry RO reject 1	100	0	32.93	102
MKR2	Pulp and paper industry RO reject 2	100	0	32.93	102
3M7BS1	Seawater (1×)	33.33	66.67	13.56	59.3
3M7BS2	Seawater (2×)	33.33	66.67	13.56	59.3
3M7BS3	Seawater (3×)	33.33	66.67	13.56	59.3
3M7BRT	Mining industry RO reject	33.33	66.67	13.56	59.3
3M7BR1	Pulp and paper industry RO reject 1	33.33	66.67	13.56	59.3
3M7BR2	Pulp and paper industry RO reject 2	33.33	66.67	13.56	59.3
BFSS1	Seawater (1×)	0	100	3.87	38
BFSS2	Seawater (2×)	0	100	3.87	38
BFSS3	Seawater (3×)	0	100	3.87	38
BFSRT	Mining industry RO reject	0	100	3.87	38
BFSR1	Pulp and paper industry RO reject 1	0	100	3.87	38
BFSR2	Pulp and paper industry RO reject 2	0	100	3.87	38

The pore solution was extracted from 1-, 7-, and 28-day-old samples (BFS2 and BFS3) using a titanium cylinder with an inner diameter of 6.5 cm, outer diameter of 16 cm, and height of 28 cm. A maximum pressure of 400 MPa was applied using an Instron 3000 universal testing machine. The pore solution was filtered with a syringe filter of 0.45 μm pore size, diluted with ultrapure water immediately after filtration, and the pH was measured. The concentrations of Ca^{2+}, Na^{+}, Cl^{-} and SO_4^{2-} were detected similarly as described above.

Table 2
Concentrations of salts in the simulated seawaters and reject waters. The concentrations of reverse osmosis (RO) reject waters were determined by optical emission spectroscopy analysis, whereas the concentrations of seawaters were reported on the basis of the standard ASTM D1141–98.

Constituent (mg/L)	Simulated seawater	Simulated seawater (2× concentration)	Simulated seawater (3× concentration)	Mining RO reject water	Pulp and paper RO reject water 1	Pulp and paper RO reject water 2
Cl^{-}	19841.41	39682.82	59524.23	50	42	790
SO_4^{2-}	2884.94	5769.88	8654.82	3100	46	290
TOC	–	–	–	3.4	4.9	35
NO_3^{-}	–	–	–	100	4.4	0.68
B^{3+}	4.71	9.42	14.13	0.12	<0.1	<0.1
Ba^{2+}	–	–	–	0.1	0.027	<0.025
Ca^{2+}	416.33	832.66	1248,99	1100	39	480
Cu^{2+}	–	–	–	<0.025	<0.025	<0.025
Mg^{2+}	1327	2654	3981	20	4.5	17
Mn^{2+}	–	–	–	0.087	<0.025	0.22
Na^{+}	11022.76	22045.52	33068.28	260	40	760
Pb^{2+}	–	–	–	<0.075	<0.075	<0.075
Sr^{2+}	13.91	27.82	41.73	2.3	0.1	1.6
Zn^{2+}	–	–	–	<0.05	<0.05	<0.05

3. Results and discussion

3.1. Identifying the fate of salts in hardened pastes

In this section, the sinks of the salts introduced to the AAMs via high-salinity waters are discussed on the basis of the XRD, EPMA, pore solution, and leaching experiments. Potential sinks could include the formation of new amorphous or crystalline mineral phases containing salt ions, chemical inclusion of salt cations or anions, or both, in aluminosilicate gels (or other phases) formed upon alkali activation, or pore solution (i.e., physical entrapment).

3.1.1. XRD

The diffractograms of the low-Ca AAMs (i.e., based on MK) are shown in Fig. 1A. It is notable that unlike in typical sodium silicate-activated MK geopolymers, several crystalline phases are present even when using deionized water. Zeolite X ($Na_2Al_2Si_{2.5}O_9{\cdot}6.2H_2O$, PDF no. 00-038-0237) and Linde B1 zeolite ($Na_{12}Al_{12}Si_{12}O_{48}{\cdot}27H_2O$, PDF no. 00-047-0162) phases were generated in all MK-containing hardened pastes. It has been suggested in the earlier literature that when NaOH is used as an activator for MK, it catalyzes the formation of zeolite $Q^4(4Al)$ crystallites, and even a modest concentration of sodium silicate in the NaOH activator greatly reduces crystallization [21–23]. The zeolite phase is capable of immobilizing cations [24]. The zeolite phase found in

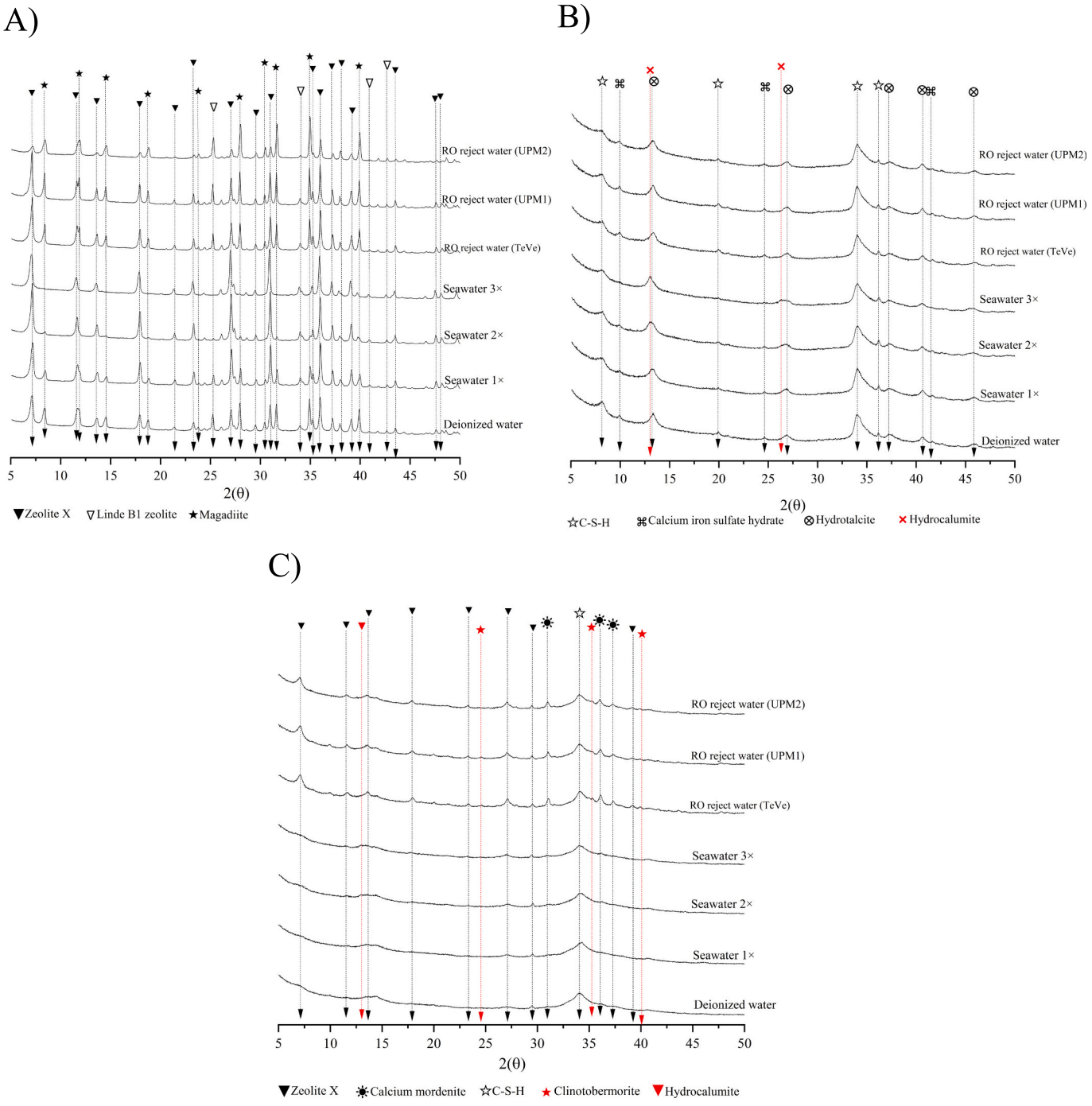

Fig. 1. XRD patterns of (A) low-Ca, (B) high-Ca, and (C) medium-Ca systems. The phases with red symbols were not observed in the reference sample prepared with deionized water.

the MKS3 sample (i.e., with the highest water salinity) was LSX zeolite ($Na_{96}Al_{96}Si_{96}O_{384}{\cdot}384.3H_2O$). Another phase formed in all low-Ca AAMs is magadiite ($Na(SiO_2)_6(OH)$, PDF no. 01-073-8410). Magadiite peak intensities decreased systematically when the salinity of synthetic seawater increased and disappeared completely in the MKS3 sample. Magadiite is formed by the self-condensation of soluble silicates, which are not involved in the formation of alkali-activated gels [25]. Thus, this result implied that silicate availability was enhanced for the alkali-activated gels (and possibly for the zeolite phases, as mentioned above) upon increasing salinity.

The XRD patterns of high-Ca system AAMs indicated the presence of a calcium silicate hydrate ($CaO{\cdot}SiO_2{\cdot}H_2O$, i.e., C–S–H, PDF no. 00-034-0002) (Fig. 1B). C–S–H is one of the main binding phases commonly encountered in alkali-activated high-Ca systems, such as when using BFS as a raw material and NaOH as an activator [10,47]. Additional Ca^{2+} was also provided by the high-salinity waters. C–S–H is a hydrated defective tobermorite analog with a nanocrystalline structure. While two silica pairs with the calcium oxide sheet, the third silica occupies a bridging position, not directly connecting to the calcium oxide sheet [26]. In comparison with natural zeolites, C–S–H products have a lower cation exchange capacity [27]. However, the C–S–H gel can physisorb chloride ions [28]. Hydrotalcite ($Mg_6Al_2(OH)_{16}{\cdot}4H_2O$, PDF no. 00-014-0191) was another phase present in all high-Ca samples. This phase is formed because of the high magnesium content of BFS [29]. Alkali-activated BFS can also contain hydrotalcite-like phases that are undetectable by XRD because of their poor crystallinity [30]. When the highest-salinity water was used (i.e., sample BFSS3), hydrocalumite ($Ca_4Al_2O_6Cl_2{\cdot}10H_2O$, PDF no. 00-019-0202) was formed, indicating partial chemical binding of chloride to the newly formed crystalline minerals. Layered double hydroxide (LDH) structures (i.e., hydrotalcite and hydrocalumite) are well known to uptake anions into their interlayer space [31]. In addition, calcium iron sulfate hydrate ($Ca_4Fe_2S_2O_9{\cdot}12(H_2O)$, PDF no. 00–044–0601) which have been concluded to have spectral similarities to ettringite in an earlier AAM study was identified [48]. The source of iron for this phase could be the trace amounts of metallic iron present in BFS or contamination from the steel molds used for casting the samples.

In the medium-Ca system (Fig. 1C), the samples prepared with RO reject concentrates (i.e., 3M7BRT, 3M7BR1, and 3M7BR2) were more crystalline than those prepared with deionized water or synthetic seawater (i.e., 3M7B, 3M7BS1, 3M7BS2, or 3M7BS3). Similar to the low-Ca system, the zeolite X phase is present in all medium-Ca system samples. One of the phases formed with RO reject waters was clinotobermorite ($[Ca_4Si_6O_{17}{\cdot}2H_2O]{\cdot}(Ca{\cdot}3H_2O)$, PDF no. 00-045-1479), which is a crystalline monoclinic form of C–S–H. Therefore, a possible explanation for the sharper peaks of clinotobermorite observed with pastes prepared with RO reject waters compared with samples prepared with deionized water and seawater could be the larger amount of dissolved calcium in RO reject water (especially RO reject from mining industry) than in seawater or deionized water. In addition to clinotobermorite, C-S-H phase appeared in all medium-Ca samples. In Table 2, the amount of sodium compared with that of Ca^{2+} in reject waters is lower than that in seawater. Similarly, as with the high-Ca system, a hydrocalumite phase was formed in the 3M7BS2 and 3M7BS3 samples. Calcium mordenite ($CaAl_2Si_{10}O_{24}{\cdot}7H_2O$) (PDF no. 00-011-0155) zeolite was also identified in all sample patterns with sharper peaks in 3M7BRT, 3M7BR1, and 3M7BR2.

3.1.2. Efflorescence formation

The efflorescence formation on the samples prepared using deionized water and seawater with 3× concentration (shown in Fig. 2) indicated that ions (e.g., Na^+ and OH^-) could migrate freely to the surface of the sample upon capillary action and react with CO_2 from the atmosphere. In general, this phenomenon can be encountered when using a highly concentrated alkali activator. However, in this study, the commonly used design criteria of AAMs were used: the molar ratio of Al/Na was ≥1 for the MK-based mix designs and the Na_2O equivalent was ≤5.5 wt% of the precursor for the BFS-based mix designs [49,50]. However, previous studies have indicated that the efflorescence formation does not cause durability issues but mainly affects the appearance of AAMs [51].

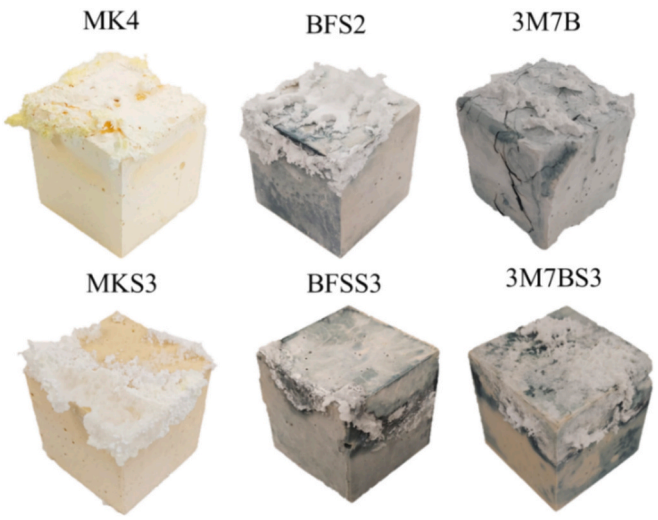

Fig. 2. Efflorescence formation on paste samples (50 × 50 × 50 mm^3) prepared with deionized water (MK4, BFS2, and 3M7B) or simulated seawater (3× concentration) (MKS3, BFSS3, and 3M7BS3).

When using deionized water, the efflorescence consisted of commonly encountered sodium carbonate (Na_2CO_3) and sodium bicarbonate ($NaHCO_3$) in all samples. However, in the low-Ca system, the efflorescence also contained sodium chloride (NaCl) in MKS2, MKS3, and 3M7BS2, whereas sodium sulfate (Na_2SO_4) was formed in 3M7BS3 (Fig. S3 in the supplementary material) indicating that in the matrix, there were no phases that were able to immobilize chloride or sulfate anions effectively. In the high-Ca system, there were no phases other than Na_2CO_3 and $NaHCO_3$, even when using high-salinity waters. Moreover, the efflorescence formation was clearly less intense with simulated seawater (3× concentration) than with deionized water or low and medium-Ca samples. A possible explanation is that using BFS as a precursor in the AAM preparation may lead to a smaller porosity than with MK or MK/BFS, which decreases efflorescence formation [32]. Additionally, the formation of hydrocalumite with high-salinity water may further decrease porosity. The high-Ca system was also able to bind salt ions more stably (as indicate by the lack of NaCl), likely due to the formation of LDH and C–S–H phases with anion adsorption properties (Fig. 1). In the medium-Ca system, NaCl phases were observed by XRD analysis of efflorescence (Fig. S3 in the supplementary material). In these samples, the mineralogy is a mixture of low and high-Ca systems (Fig. 1C); thus, the low-Ca phases (zeolite and zeolite-like phases) are unable to immobilize chloride. Moreover, the medium-Ca sample prepared with deionized water exhibited cracks, indicating low durability when in contact with water.

3.1.3. Leaching experiments on monolithic samples

The leaching experiments on monolithic samples were used to assess whether the salts can migrate out of the AAM structures when exposed to water. Here, only the high-Ca mix design is considered (because of the promising performance in the efflorescence test), and the most highly concentrated water type (i.e., seawater with 3× concentration) is compared with deionized water. The leaching of the main elements or ions, that is, Ca^+, Na^+, SO_4^{2-}, and Cl^- (as weight percentage of the total element amount in the mix designs) are shown in Fig. 3.

The leaching of Ca^{2+}, Na^+, and SO_4^{2-} from the sample prepared with seawater with 3× concentration (i.e., BFSS3) is either lower or on a similar level when compared with that from the sample prepared with

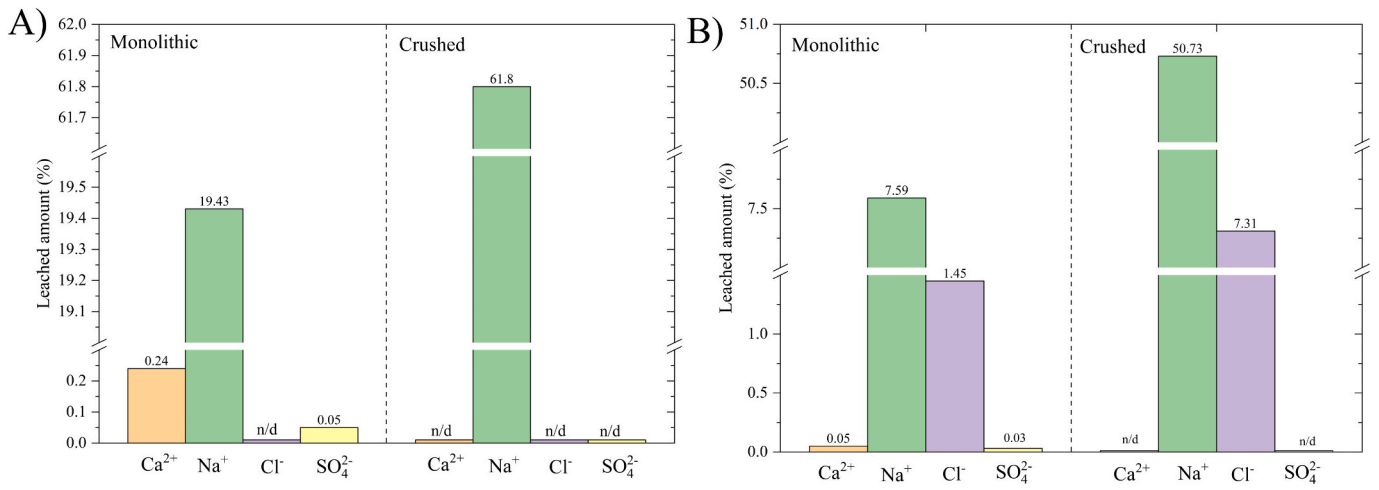

Fig. 3. Leached amount (as weight%) of elements and ions in (A) BFS2 and (B) BFSS3. The leached amount was calculated as the ratio of the weight of the element or ion in the solution after the leaching test to the total weight of the element or ion in the paste sample.

deionized water (i.e., BFS2). This indicates that the nano/microstructure of BFSS3 hinders the mobility of Ca^{2+}, Na^{+}, and SO_4^{2-} as supported by the efflorescence formation. When comparing the crushed and monolithic samples, the former has higher leaching than the latter due to its large exposed surface area.

For Cl^{-}, <2 % (monolithic sample) and 7 % (crushed sample; Table S1 in the supplementary material) leached out of the material prepared with seawater (3× concentration), which indicates very efficient immobilization. Some of the Cl^{-} ions were likely taken up by hydrocalumite or hydrotalcite (which were identified by XRD) via anion exchange [31].

SO_4^{2-} was also stabilized effectively (maximum 0.05 wt% leaching). Part of SO_4^{2-} is immobilized into calcium iron sulfate hydrate (Fig. 1) with low water solubility. Therefore, increasing the BFS content (i.e., source of Ca^{2+}) in the matrix can be a practical way to stabilize sulfate [33].

The leaching of Ca^{2+} is lower in the BFSS3 sample than in the reference sample (i.e., BFS2). Ca^{2+} is a crucial element in the C–(A)–S–H gel, and its incorporation is stable. This stability ensures that the release of Ca^{2+} from the gel is limited [17]. An additional sink of Ca^{+} could be the hydrocalumite phase, as identified by XRD.

The leaching of Na^{+} is higher than that of other elements. In general, Na^{+} is associated with its ability to compensate for charge with tetrahedral Al^{3+} sites (i.e., $[AlO_4]^{-}$) in AAM systems. The leaching of Na^{+} indicates that the alkali activator might have been too concentrated, even though the binder was designed according to guidelines, as stated above.

3.1.4. Pore solution

The high-Ca samples prepared with deionized water (i.e., BFS2) and seawater with 3× concentration (i.e., BFSS3) were chosen for pore solution extraction, which was performed from 1, 7, and 28-day cured samples. As BFS dissolves in the NaOH solution and new mineral phases are formed, either water from the activator is chemically bound into the reaction products (i.e., hydration occurs), or it remains as free (or evaporable) water forming the pore solution. Pore solution analysis provides information about the dissolved ions remaining physically immobilized in the AAM matrix in free water.

The concentration of Ca^{2+} was low in the pore solution of both samples (BFS2 and BFSS3), indicating that the formed gel phases effectively incorporated Ca^{2+} ions from both the dissolved precursor and seawater, as can be seen from Table 4. The concentration of Na^{+} is only approximately 600–900 mg/L higher in BFSS3 than in BFS2 (in the latter, the Na^{+} source is only the alkali activator). This is significantly lower than the initial concentration of seawater (which was ~25000 mg Na^{+}/L); thus, >96 % of Na^{+} is incorporated into the solid phases either as a part of the chemical structure or adsorbed upon the surface. The same applies for Cl^{-}, where the concentration is approximately 98 % lower than that in the seawater pristine solution. For SO_4^{2-}, the difference between BFS2 and BFSS3 is unclear because there was fluctuation in the concentrations of BFS2 over time. Overall, the temporal trends indicated a decrease in the Na^{+} concentration with BFS2, whereas with BFSS3, the concentrations of Na^{+}, Cl^{-}, and SO_4^{2-} appear to increase as the curing time increased. Unfortunately, it was not possible to extract any pore solution from the 28-day-cured BFSS3 sample due to blocked pores or a less porous microstructure.

Interestingly, the pH of BFSS3 appears to be higher than that of BFS2 at the 1-day age, even though both BFS2 and BFSS3 were prepared with a similar concentration of NaOH. The pH of the pore solution reflects the conditions during the alkali activation process where OH^{-} ions act catalytically [34] and higher pH enhances the dissolution of the aluminosilicate precursor [35,36]. The higher pH of the BFSS3 pore solution may be reflected in the higher early age (1 and 7 day) compressive strength of BFSS3 compared with that of BFS2 (Fig. 5).

3.1.5. Elemental mapping of the binders

Elemental mapping (Fig. 4) was conducted to visualize the changes in binder compositions when changing the water type. In the low-Ca system (other samples than MKR2), the increase in water salinity and the use of RO reject waters result in a more even distribution of Al^{3+} and Si^{4+}, indicating an enhanced dissolution of MK. This can be observed by more intense yellow color (i.e., approx. 10 or 18 % of Si and Al,

Table 4
Compositions of pore solutions of high-Ca paste prepared with deionized water (i.e., BFS2) and triple concentrated seawater (i.e., BFSS3) over time.

Time (day)	BFS2					BFSS3				
	Ca^{2+} (mg/L)	Na^{+} (mg/L)	Cl^{-} (mg/L)	SO_4^{2-} (mg/L)	pH	Ca^{2+} (mg/L)	Na^{+} (mg/L)	Cl^{-} (mg/L)	SO_4^{2-} (mg/L)	pH
1	<0.5	780	<2.5	100	12.1	<0.5	1400	1100	170	12.3
7	<0.25	750	<2.5	58	12.1	<0.27	1600	1200	180	12.2
28	0.24	680	<2.5	190	12.5	–	–	–	–	–

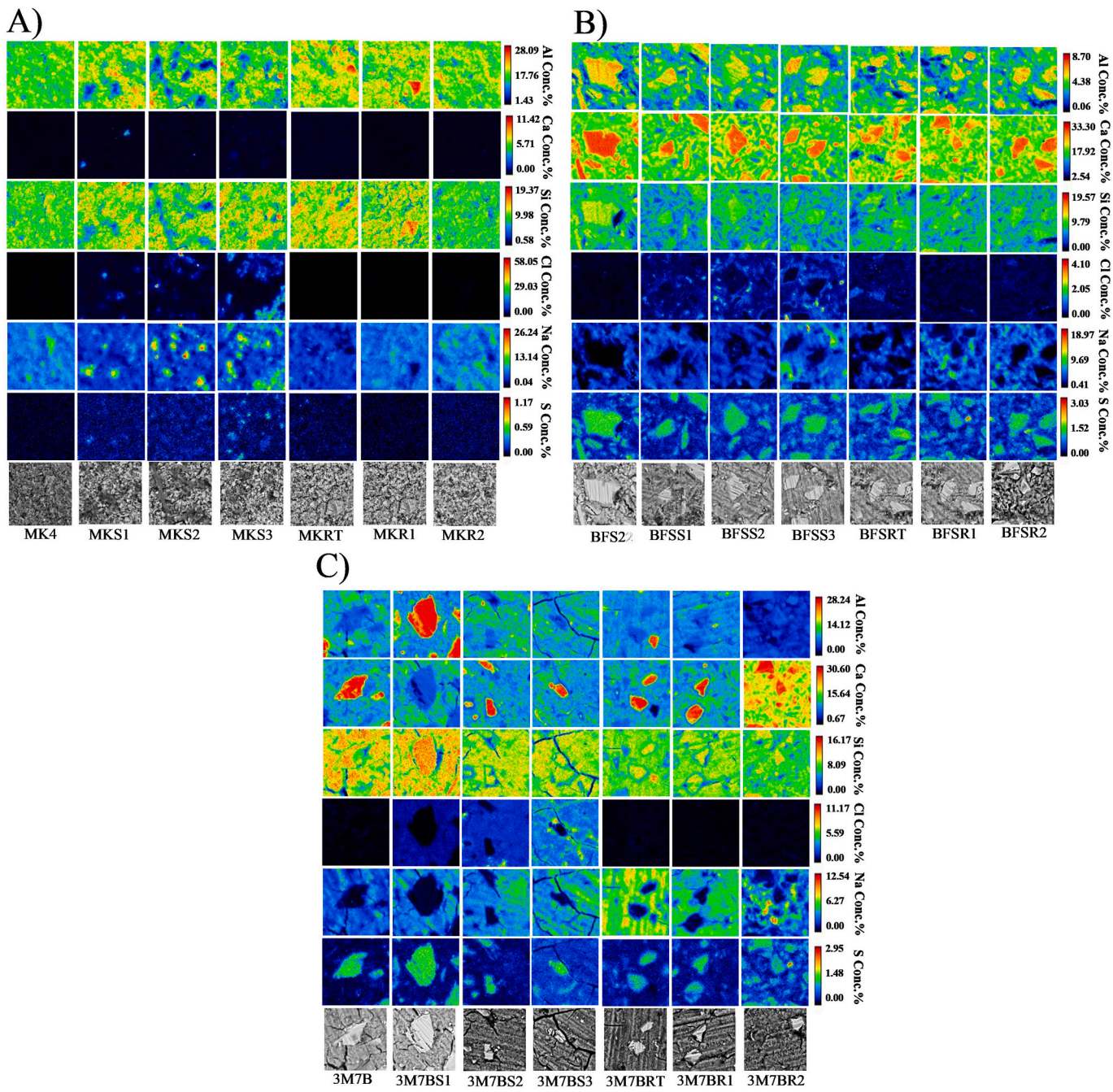

Fig. 4. EPMA analysis results as concentrations of (A) low-Ca, (B) high-Ca, and (C) medium-Ca systems.

respectively) distribution. According to the Cl^- and Na^+ maps, the highest concentrations of these elements in the MKS1, MKS2, and MKS3 samples appear in the same areas, confirming the presence of NaCl.

In the high-Ca system (i.e., BFS), the most obvious changes upon increasing the salt content are an increase in the binder Ca^{2+} content and a decrease in the Si^{4+} content. Interestingly, there are Na-rich areas in the elemental maps, which are not accompanied by high Cl^- or S contents, indicating that the gel itself has taken up Na^+ or that carbonated phases exist. In particular, BFSS1, BFSS2, and BFSS3, Cl^- is present in the same areas as Ca^{2+} and Al^{3+}, which is likely related to the presence of the hydrocalumite phase.

In the medium-Ca system (i.e., a mixture of MK and BFS), the dissolution of Al^{3+} and Si^{4+} might have been enhanced, as can be proven by the high overall concentrations of these elements in the binder. Interestingly, the Ca^{2+} content in the binder is much higher with 3M7BR2 compared with other samples. Ca^{2+}, Al^{3+}, and Cl^- are present in the same areas, which is evidence of the existence of the hydrocalumite phase, as observed using XRD.

3.2. Evaluation of binders as construction materials

3.2.1. Compressive strength results

Curing times of 1 and 7 days using simulated seawater solutions in the mix designs led to an increase in compressive strength for all precursors compared with that of samples prepared with deionized water (Fig. 5). Alkali activator composition affects the mechanical properties of AAMs by influencing their dissolution behavior [37]. A possible explanation for dissolution improvement is the enhanced dissolution of precursors upon using saltwater due to mechanisms similar to those using sodium sulfate-based alkali activators [38]. The exact mechanism

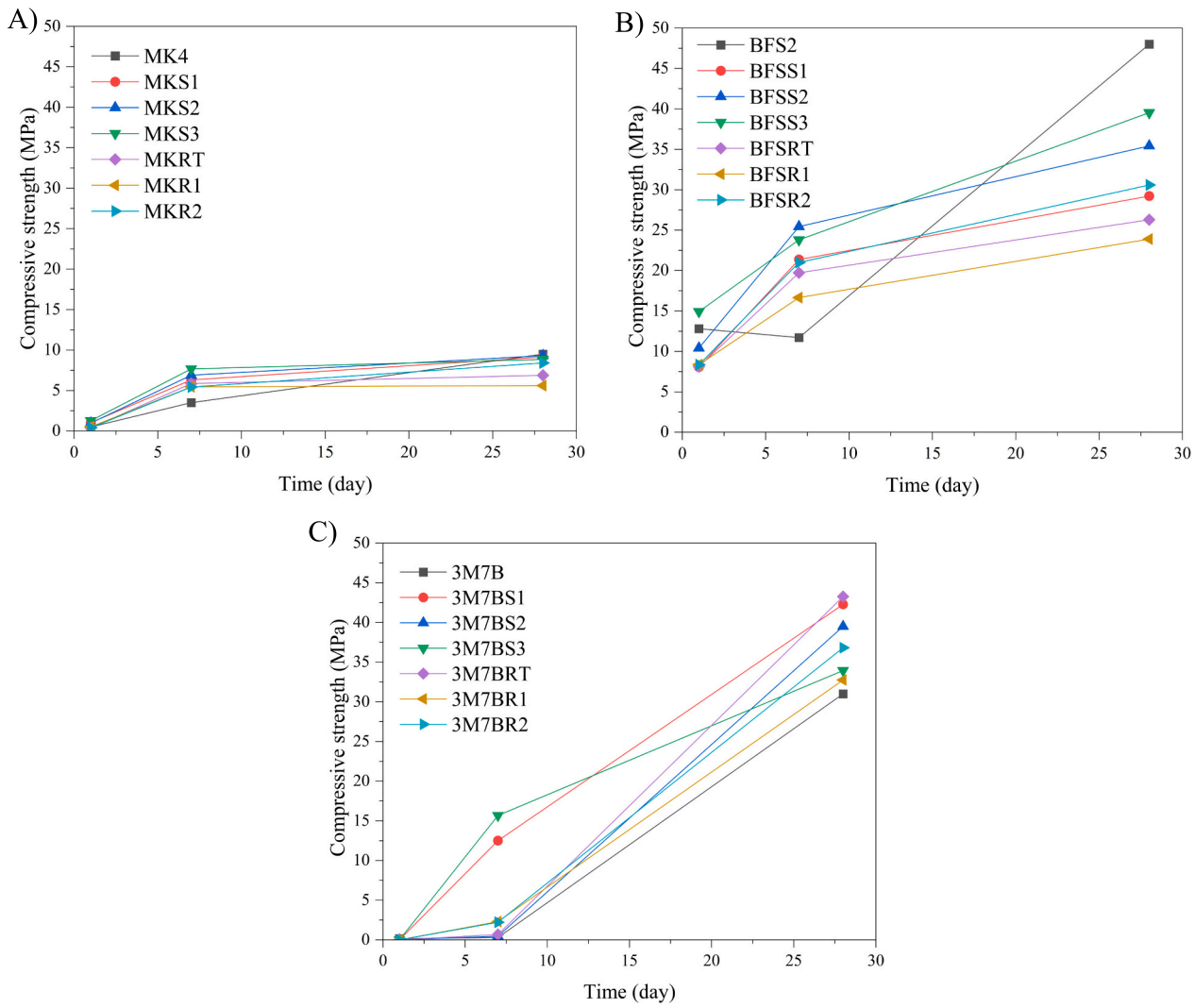

Fig. 5. Compressive strength of 1-, 7-, and 8-day old (A) low-Ca, (B) high-Ca, and (C) medium-Ca systems.

of sulfate-based alkali activation is unclear in the literature, but one hypothesis could be the enhanced formation of Ca^{2+}–SO_4^{2-} ion-pair complexes at high SO_4^{2-} concentration, which may drive the enhanced dissolution of Ca-rich precursors, such as BFS. The formation of Ca^{2+}–SO_4^{2-} ion-pair complexes may be considered an intermediate step before the nucleation of solid phases [39]. There is a correlation between the presence of Cl^-, SO_4^{2-}, and Na^+ ions and the acceleration of gel formation, as well as the pore-filling effects from the crystallization of salts that may also contribute to the initial compressive strength enhancement [40,41].

The compressive strength of 28-day-old hardened samples prepared with high-salinity water is lower than that of the reference sample prepared with deionized water in low and high-Ca systems. Criado et al. [42], who used sodium sulfate as an alkali activator to prepare AAMs based on low-Ca fly ash, concluded that sodium sulfate promotes crystallization of zeolites by changing reaction kinetics and interrupting gel formation, resulting in a low mechanical strength development. After 28 days, the compressive strength did not differ as clearly as it did compared with that of the reference sample at 7 days, possibly due to the negative effects (i.e., delay or interruption of gel formation) of the salts. In the case of the medium-Ca system, pastes prepared using high-salinity water had higher compressive strength than the reference samples after 28 days of curing.

One practical application of the developed binders could be as a mine backfill material, which can be used to refill excavated holes or tunnel sections in mines. Mines frequently utilize the RO process to treat their wastewaters, which results in the formation of RO reject waters. If the mine is located inland, the disposal of the reject water may be expensive or otherwise unfeasible. The final compressive strength of a backfill material can range from 0.2 to 5 MPa [43]. The materials tested here were not based on standard-sized specimens and did not contain any sand or coarse aggregates; thus, the compressive strength cannot be directly compared with that reported in the literature. Nevertheless, the compressive strength of the samples is encouraging because concrete samples typically have higher strength than paste or mortar [44].

3.2.2. *Setting time*

The setting time for all pastes prepared with high-salinity water increased in comparison with that for reference samples prepared with deionized water (Fig. 6). According to Rattanasak et al. [45], the increased amount of sulfate could cause a delay in the setting time. In their study, calcium aluminate formed ettringite on the surface of precursor particles, decreasing the dissolution of silica and alumina and resulting in delayed paste setting [45]. The XRD analysis for this study does not show ettringite, but this may be due to the low quantity of this phase. Sulfate can be additionally adsorbed on the reactive sites on the precursor surface which can delay the setting.

As an end-of-life scenario for construction materials, crushed samples can be evaluated by leaching experiments and compared with the European Council Decision 2003/33/EC (2003) (criteria and procedures

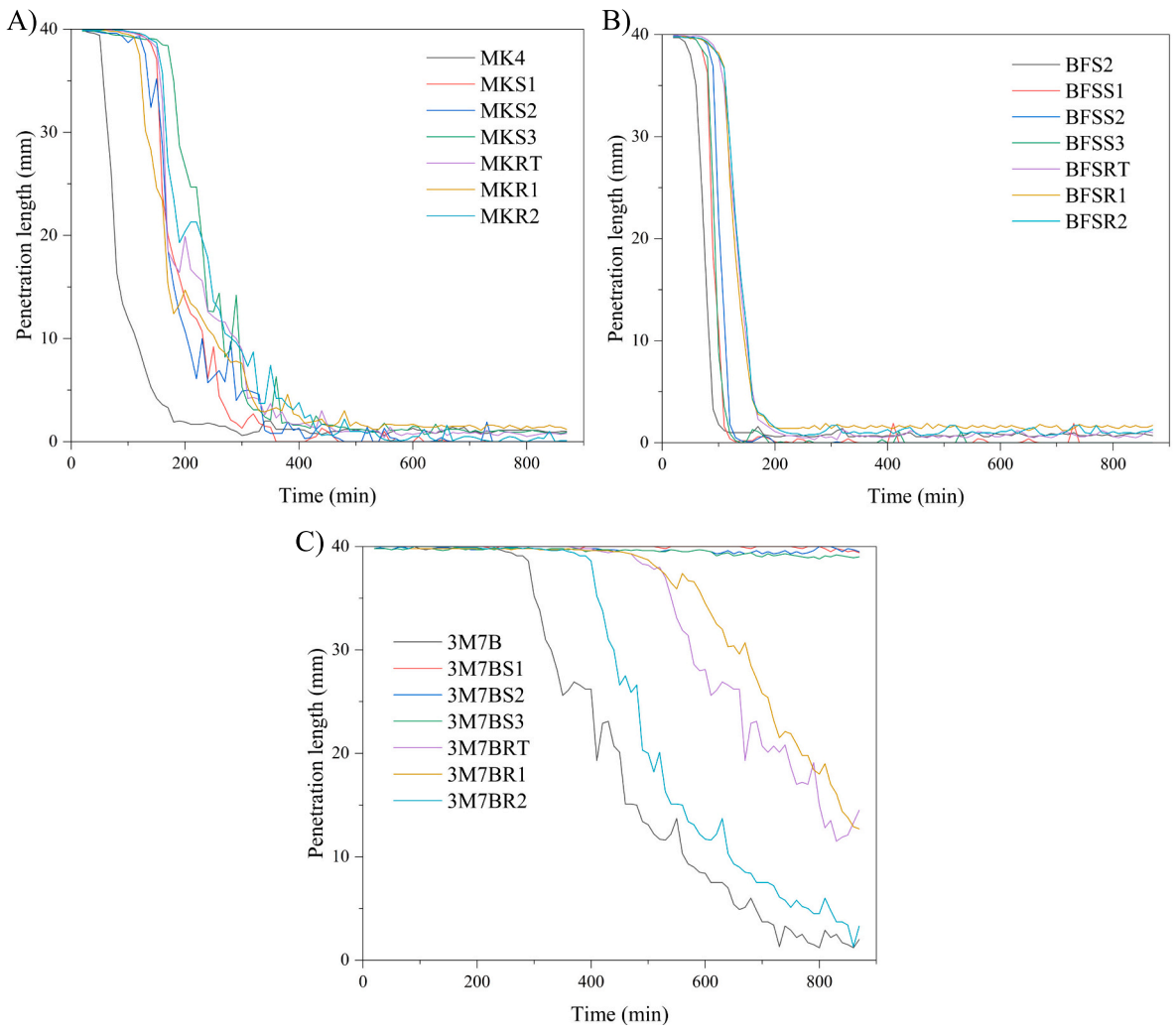

Fig. 6. Setting time graphs of the (A) low-Ca, (B) high-Ca, and (C) medium-Ca systems.

for the acceptance of waste at landfills). Of the parameters listed in the landfill criteria, only Cl^- and SO_4^{2-} are relevant to this study. Their leaching values (as mg/kg, shown in Table S1 in the supplementary material) define waste materials as inert, nonhazardous, or hazardous. According to the classification, the low and medium-Ca samples do not pass the leaching values of sulfate and chloride for inert waste, and they are nonhazardous wastes. Conversely, the high-Ca samples could be classified as inert waste.

4. Conclusions

In this study, a novel concept of immobilizing RO reject waters into an alkali-activated matrix was studied. The aims were to identify the most feasible binder chemistry (from low, medium, or high-Ca^{2+} gel compositions), understand the immobilization mechanism of salts, and evaluate the suitability of the materials for construction applications (e.g., as mine backfill material).

The following conclusions can be drawn:

(1) The high-Ca system (i.e., BFS as a precursor) performed better overall than the low-Ca system (i.e., prepared with MK) or medium-Ca system (i.e., prepared with a mixture of slag and MK) from the viewpoint of salt immobilization.
(2) The XRD patterns indicated the formation of LDH phases and hydrocalumite in the high-Ca system, zeolites in the low-Ca system, and a mixture of those in the medium-Ca system. The LDH phases likely contributed to the effective immobilization of anions (e.g., Cl^-) as indicated by efflorescence and leaching experiments. Sulfate was also immobilized into the calcium sulfate phase in the high-Ca system.
(3) Pore solution analyses indicated that only a minor fraction of the ions (Ca^{2+}, Na^+, Cl^-, and SO_4^{2-}) remained dissolved in free water.
(4) All paste samples exhibited robust compressive strength, making them suitable for various construction applications, such as mine backfilling. Additionally, the setting time increased with increasing water salinity. The crushed low and medium-Ca and high-Ca pastes could be classified as nonhazardous and inert wastes, respectively, according to European Council Decision 2003/33/EC (2003).

CRediT authorship contribution statement

Sima Kamali: Writing – original draft, Visualization, Methodology, Investigation, Formal analysis, Data curation. **Vitalii Ponomar:** Writing – review & editing, Visualization, Methodology, Investigation. **Giovanni Dal Poggetto:** Writing – review & editing, Investigation. **Cristina Leonelli:** Writing – review & editing, Supervision. **Katja Kilpimaa:** Writing – review & editing, Supervision, Methodology, Conceptualization. **Tero Luukkonen:** Writing – review & editing, Supervision, Project administration, Methodology, Funding acquisition, Conceptualization.

Declaration of competing interest

The authors declare that they have no known competing financial interests or personal relationships that could have appeared to influence the work reported in this paper.

Data availability

Data will be made available on request.

Acknowledgments

This work was financially supported by Business Finland (project CEIWA, grant ID 563/31/2021), the University of Oulu and the Academy of Finland (PROFI5, 326291), and the European Union – NextGenerationEU (project KaiPa, grant ID ESAELY/521/2022).

Appendix A. Supplementary data

Supplementary data to this article can be found online at https://doi.org/10.1016/j.desal.2024.117859.

References

[1] S.A. Miller, A. Horvath, P.J.M. Monteiro, Impacts of booming concrete production on water resources worldwide, Nature Sustainability 1 (2018) 69–76, https://doi.org/10.1038/s41893-017-0009-5.
[2] W. Lv, Z. Sun, Z. Su, Study of seawater mixed one-part alkali activated GGBFS-fly ash, Cement and Concrete Composites 106 (2020) 103484, https://doi.org/10.1016/j.cemconcomp.2019.103484.
[3] V.G. Gude, Energy consumption and recovery in reverse osmosis, Desalin. Water Treat. 36 (2011) 239–260, https://doi.org/10.5004/dwt.2011.2534.
[4] J. Morillo, J. Usero, D. Rosado, H. El Bakouri, A. Riaza, F.-J. Bernaola, Comparative study of brine management technologies for desalination plants, Desalination 336 (2014) 32–49, https://doi.org/10.1016/j.desal.2013.12.038.
[5] A. Subramani, J.G. Jacangelo, Treatment technologies for reverse osmosis concentrate volume minimization: a review, Sep. Purif. Technol. 122 (2014) 472–489, https://doi.org/10.1016/j.seppur.2013.12.004.
[6] P. Krivenko, O. Kovalchuk, A. Pasko, Utilization of industrial waste water treatment residues in alkali activated cement and concretes, Key Eng. Mater. 761 (2018) 35–38, https://doi.org/10.4028/www.scientific.net/KEM.761.35.
[7] X. Lyu, N. Robinson, M. Elchalakani, M.L. Johns, M. Dong, S. Nie, Sea sand seawater geopolymer concrete, Journal of Building Engineering 50 (2022) 104141, https://doi.org/10.1016/j.jobe. 2022.104141.
[8] C. Leonelli, A. Palomo, Chemistry and materials science of alkali-activated materials, in: Alkali-Activated Materials in Environmental Technology Applications, Elsevier, 2022, pp. 13–40, https://doi.org/10.1016/B978-0-323-88438-9.00013-2.
[9] L.B. de Oliveira, A.R.G. de Azevedo, M.T. Marvila, E.C. Pereira, R. Fediuk, C.M. F. Vieira, Durability of geopolymers with industrial waste, Case Studies in Construction Materials 16 (2022) e00839, https://doi.org/10.1016/j.cscm.2021.e00839.
[10] V. Ponomar, T. Luukkonen, J. Yliniemi, Revisiting alkali-activated and sodium silicate-based materials in the early works of Glukhovsky, Construct. Build Mater. 398 (2023) 132474, https://doi.org/10.1016/j.conbuildmat.2023.132474.
[11] B.I. El-Eswed, Solidification/stabilization of hazardous wastes by alkali activation, in: Alkali-Activated Materials in Environmental Technology Applications, Elsevier, 2022, pp. 279–313, https://doi.org/10.1016/B978-0-323-88438-9.00006-5.
[12] H. Zhang, Z. Ji, Y. Zeng, Y. Pei, Solidification/stabilization of landfill leachate concentrate contaminants using solid alkali-activated geopolymers with a high liquid solid ratio and fixing rate, Chemosphere 288 (2022) 132495, https://doi.org/10.1016/j.chemosphere.2021.132495.
[13] G.F. Huseien, A.R.M. Sam, K.W. Shah, J. Mirza, Effects of ceramic tile powder waste on properties of self-compacted alkali-activated concrete, Construct. Build Mater. 236 (2020) 117574, https://doi.org/10.1016/j.conbuildmat.2019.117574.
[14] J. Yliniemi, P. Kinnunen, P. Karinkanta, M. Illikainen, Utilization of mineral wools as alkali-activated material precursor, Materials 9 (2016) 312, https://doi.org/10.3390/ma9050312.
[15] C.C. Novo, L. Senff, M.P. Seabra, R.M. Novais, J.A. Labrincha, The role of an industrial alkaline wastewater in the alkali activation of biomass fly ash, Applied Sciences 12 (2022) 3612, https://doi.org/10.3390/app12073612.
[16] J. Xie, P. Chen, J. Li, Y. Xu, Y. Fang, A. Wang, J. Wang, Directly upcycling copper mining wastewater into a source of mixing water for the preparation of alkali-activated slag materials, Process Saf. Environ. Prot. 168 (2022) 362–371, https://doi.org/10.1016/j.psep. 2022.10.011.
[17] T. Luukkonen, J. Yliniemi, P. Kinnunen, M. Illikainen, Sustainable batching water options for one-part alkali-activated slag mortar: sea water and reverse osmosis reject water, PloS One 15 (2020) e0242462, https://doi.org/10.1371/journal.pone.0242462.
[18] C. Ponzoni, I. Lancellotti, L. Barbieri, A. Spinella, M.L. Saladino, D.C. Martino, E. Caponetti, F. Armetta, C. Leonelli, Chromium liquid waste inertization in an inorganic alkali activated matrix: leaching and NMR multinuclear approach, J. Hazard. Mater. 286 (2015) 474–483, https://doi.org/10.1016/j.jhazmat.2014.12.054.
[19] M. Giorgetti, M. Berrettoni, G. Aquilanti, G. Boldrini, I. Lancellotti, C. Leonelli, The coordination core and charge of chromium in metakaolin-geopolymers as revealed by X-ray absorption spectroscopy, Mater. Lett. 270 (2020) 127741, https://doi.org/10.1016/j.matlet.2020.127741.
[20] Standard Practice for the Preparation of Substitute Ocean Water, 2003.
[21] Q. Wan, F. Rao, S. Song, R.E. García, R.M. Estrella, C.L. Patiño, Y. Zhang, Geopolymerization reaction, microstructure and simulation of metakaolin-based geopolymers at extended Si/Al ratios, Cement and Concrete Composites 79 (2017) 45–52, https://doi.org/10.1016/j.cemconcomp.2017.01.014.
[22] B. Zhang, K.J.D. MacKenzie, I.W.M. Brown, Crystalline phase formation in metakaolinite geopolymers activated with NaOH and sodium silicate, J. Mater. Sci. 44 (2009) 4668–4676, https://doi.org/10.1007/s10853-009-3715-1.
[23] Z. Zhang, H. Wang, J.L. Provis, F. Bullen, A. Reid, Y. Zhu, Quantitative kinetic and structural analysis of geopolymers. Part 1. The activation of metakaolin with sodium hydroxide, Thermochim. Acta 539 (2012) 23–33, https://doi.org/10.1016/j.tca.2012.03.021.
[24] Z. Xu, Z. Jiang, D. Wu, X. Peng, Y. Xu, N. Li, Y. Qi, P. Li, Immobilization of strontium-loaded zeolite A by metakaolin based-geopolymer, Ceram. Int. 43 (2017) 4434–4439, https://doi.org/10.1016/j.ceramint.2016.12.092.
[25] F. Li, Y. Lu, Z. Liu, L. Shan, Reverse-diffusion phenomenon of high ductility fly ash-based geopolymer against carbonation, Ceram. Int. 49 (2023) 28954–28964, https://doi.org/10.1016/j.ceramint.2023.06.164.
[26] E. Bernard, Y. Yan, B. Lothenbach, Effective cation exchange capacity of calcium silicate hydrates (C-S-H), Cem. Concr. Res. 143 (2021) 106393, https://doi.org/10.1016/j.cemconres. 2021.106393.
[27] S. Komarneni, D.M. Roy, Tobermorites: a new family of cation exchangers, Science 221 (1983) 647–648, https://doi.org/10.1126/science.221.4611.647.
[28] J. Yang, D. Hou, Q. Ding, Ionic hydration structure, dynamics and adsorption mechanism of sulfate and sodium ions in the surface of calcium silicate hydrate gel: a molecular dynamics study, Appl. Surf. Sci. 448 (2018) 559–570, https://doi.org/10.1016/j.apsusc.2018.04.071.
[29] J.L. Provis, S.A. Bernal, Geopolymers and related alkali-activated materials, Annu. Rev. Mat. Res. 44 (2014) 299–327, https://doi.org/10.1146/annurev-matsci-070813-113515.
[30] M. Komljenović, G. Tanasijević, N. Džunuzović, J.L. Provis, Immobilization of cesium with alkali-activated blast furnace slag, J. Hazard. Mater. 388 (2020) 121765, https://doi.org/10.1016/j.jhazmat.2019.121765.
[31] Y. Jun, S. Yoon, J. Oh, A comparison study for chloride-binding capacity between alkali-activated fly ash and slag in the use of seawater, Appl. Sci. 7 (2017) 971, https://doi.org/10.3390/app 7100971.
[32] Z. Zhang, J.L. Provis, A. Reid, H. Wang, Fly ash-based geopolymers: the relationship between composition, pore structure and efflorescence, Cem. Concr. Res. 64 (2014) 30–41, https://doi.org/10.1016/j.cemconres.2014.06.004.
[33] J. Kiventerä, H. Sreenivasan, C. Cheeseman, P. Kinnunen, M. Illikainen, Immobilization of sulfates and heavy metals in gold mine tailings by sodium silicate and hydrated lime, J. Environ. Chem. Eng. 6 (2018) 6530–6536, https://doi.org/10.1016/j.jece.2018.10.012.
[34] I. Garcia-Lodeiro, A. Palomo, A. Fernández-Jiménez, An overview of the chemistry of alkali-activated cement-based binders, in: Handbook of Alkali-Activated Cements, Mortars and Concretes, Elsevier, 2015, pp. 19–47, https://doi.org/10.1533/9781782422884.1.19.
[35] W. Chen, R. Peng, C. Straub, B. Yuan, Promoting the performance of one-part alkali-activated slag using fine lead-zinc mine tailings, Construct. Build Mater. 236 (2020) 117745, https://doi.org/10.1016/j.conbuildmat.2019.117745.
[36] Y. Zuo, M. Nedeljković, G. Ye, Pore solution composition of alkali-activated slag/fly ash pastes, Cem. Concr. Res. 115 (2019) 230–250, https://doi.org/10.1016/j.cemconres.2018.10.010.
[37] V. Ponomar, J. Yliniemi, E. Adesanya, K. Ohenoja, M. Illikainen, An overview of the utilisation of Fe-rich residues in alkali-activated binders: mechanical properties and state of iron, J. Clean. Prod. 330 (2022) 129900, https://doi.org/10.1016/j.jclepro.2021.129900.
[38] A.M. Rashad, Y. Bai, P.A.M. Basheer, N.B. Milestone, N.C. Collier, Hydration and properties of sodium sulfate activated slag, Cement and Concrete Composites 37 (2013) 20–29, https://doi.org/10.1016/j.cemconcomp.2012.12.010.
[39] R.J. Myers, G. Geng, J. Li, E.D. Rodríguez, J. Ha, P. Kidkhunthod, G. Sposito, L. N. Lammers, A.P. Kirchheim, P.J.M. Monteiro, Role of adsorption phenomena in cubic tricalcium aluminate dissolution, Langmuir 33 (2017) 45–55, https://doi.org/10.1021/acs.langmuir.6b03474.
[40] Y. Jun, S.H. Han, Y.H. Bae, J.H. Kim, Seawater-mixed alkali-activated materials: a comparative investigation of metal slag suitability, J. Sustain. Cem.-Based Mater. 12 (2023) 907–923.
[41] A.M. Rashad, M. Ezzat, A preliminary study on the use of magnetic, Zamzam, and sea water as mixing water for alkali-activated slag pastes, Construct. Build Mater. 207 (2019) 672–678, https://doi.org/10.1016/j.conbuildmat.2019.02.162.
[42] M. Criado, A.F. Jiménez, A. Palomo, Effect of sodium sulfate on the alkali activation of fly ash, Cem. Concr. Compos. 32 (2010) 589–594, https://doi.org/10.1016/j.cemconcomp.2010.05.002.
[43] M. Falah, K. Ohenoja, R. Obenaus-Emler, P. Kinnunen, M. Illikainen, Improvement of mechanical strength of alkali-activated materials using micro low-alumina mine tailings, Construct. Build Mater. 248 (2020) 118659, https://doi.org/10.1016/j.conbuildmat.2020.118659.

[44] F. Collins, J.G. Sanjayan, Early age strength and workability of slag pastes activated by sodium silicates, Mag. Concr. Res. 53 (2001) 321–326, https://doi.org/10.1680/macr.2001.53.5.321.
[45] U. Rattanasak, K. Pankhet, P. Chindaprasirt, Effect of chemical admixtures on properties of high-calcium fly ash geopolymer, Int. J. Miner. Metall. Mater. 18 (2011) 364–369, https://doi.org/10.1007/s12613-011-0448-3.
[47] C.K. Yip, G.C. Lukey, J.S. Van Deventer, The coexistence of geopolymeric gel and calcium silicate hydrate at the early stage of alkaline activation, Cem. Concr. Res. 35 (9) (2005) 1688–1697, https://doi.org/10.1016/j.cemconres.2004.10.042.
[48] S. Serrano, D. Vlassopoulos, Mechanism of Hg (II) immobilization in sediments by sulfate-cement amendment, Appl. Geochemistry 67 (2016) 68–80, https://doi.org/10.1016/j.apgeochem.2016.01.007.
[49] J.L. Provis, J.S. Van Deventer (Eds.), Alkali activated materials: state-of-the-art report, RILEM TC 224-AAM (Vol. 13), Springer Science & Business Media, 2013, https://doi.org/10.1007/978-94-007-7672-2.
[50] S.D. Wang, K.L. Scrivener, P.L. Pratt, Factors affecting the strength of alkali-activated slag. Cem. Concr. Res. 24 (6) (1994) 1033–1043, https://doi.org/10.1016/0008-8846(94)90026-4.
[51] P. Cong, Y. Cheng, Advances in geopolymer materials: a comprehensive review, J. Traffic Transp. Eng. (English Edition) 8 (3) (2021) 283–314, https://doi.org/10.1016/j.jtte.2021.03.004.